

THz Low Resolution Spectroscopy for Astronomy

Gordon J. Stacey

Abstract—The THz spectral regime provides a wide range of spectral lines that are invaluable probes of star formation and AGN activity in galaxies both in the local Universe and at the earliest times. We review the utility of these lines, give examples of the science they deliver, and detail the properties of successful low resolution direct detection spectrometers for work in the THz regime. We finish with a discussion of the exciting new science we expect with the next direct detection generation spectrometers on new facilities such as SOFIA, CCAT, SPICA, and ALMA.

Index Terms—direct detection receivers, extragalactic spectroscopy, fine-structure lines, TH spectroscopy

I. INTRODUCTION

THE THz spectrum, here loosely defined as frequencies between 600 GHz and 6 THz, contains a plethora of readily detectable spectral lines that are important diagnostics for both the physical and chemical conditions of the gas and the sources of energy within astrophysical environments. These spectral probes include rotational lines from simple molecules (e.g. HD, CH, OH, CO, NH₃, H₂O), and the ground state fine-structure lines from abundant atoms and ions. These lines are well explored in both galactic and extragalactic environments, and indeed the molecular lines can be important probes of planetary atmospheres in the solar system. Important results are obtained with both coherent (heterodyne) and incoherent (direct detection) spectrometers. Here we focus on work done with direct detection spectrometers whose natural niche is the broad spectral line environment of extragalactic studies. In this context, line widths are ~50 to 500 km/sec, the smaller values typical for low mass dwarf galaxies and spiral galaxies viewed “face-on” and the larger values more typical for more massive systems with more arbitrary presentations on the sky. This narrows our focus to the lines with large luminosities on galactic scales, these are the lines that are important coolants of the interstellar medium (ISM) including the fine-structure lines of C, C⁺, N⁺, N⁺⁺, O, and O⁺⁺, and the mid-J rotational lines of CO.

This paper is divided into five sections. Following this introduction, Sec. II discusses these spectral lines and their utility as probes of astrophysical environments, Sec. III is a brief history of observations of these lines which also

summarizes some exciting new astrophysical discoveries, Sec. IV is a discussion of the merits of direct detection systems, Sec. V gives examples of moderate resolving power direct detection systems that are used for astrophysical experiments today, and Sec. VI discusses some of the prospects for future work.

II. ASTROPHYSICAL PROBES WITHIN THE THz BANDS

A. Fine-Structure Lines

Atoms or ions with ground state electronic configurations that contain valence electrons will have their configurations ordered by the residual electrostatic interaction into terms that differ in the total (vector) orbital angular momentum ($\mathbf{L} \equiv \sum \mathbf{l}_i$) and total (vector) spin angular momentum ($\mathbf{S} \equiv \sum \mathbf{s}_i$). These terms are denoted by ^{2S+1}P , where the superscript $2S+1$ is equivalent to the number of levels into which the term is split, and P denotes the total orbital angular momentum of the electronic term and follows the usual convention where S,P,D,F... refer to terms of $L = 0,1,2,3,\dots$. These terms are further split by the spin-orbit interaction into levels $^{2S+1}P_J$ where the subscript J denotes the magnitude of the vector sum of \mathbf{L} and \mathbf{S} : $\mathbf{J} \equiv \mathbf{L} + \mathbf{S}$. Each of these levels, J, has a degeneracy given by $g_J = 2J+1$. When an atom or ion has 1, 2, 4, or 5 equivalent p electrons in its ground state configuration, the ordering and selection rules dictate that its ground state term will be 3P or 2P terms, so that it has ground state fine-structure lines. After H and He, which have no low-lying energy levels, the three most abundant elements in the Universe are oxygen, carbon, and nitrogen with relative abundances ~ 6, 3, and 1×10^{-4} with respect to hydrogen respectively. Amongst these elements, the O, O⁺⁺, C, C⁺, N⁺, and N⁺⁺ ionization states have ground term split into fine-structure levels that emit photons in the THz range (Table 1). Since transitions within a term involve no change in the electronic configuration, they are forbidden to electronic dipole radiation and decay by magnetic dipole transitions. As such, the excited fine-structure levels are metastable with lifetimes measured in days.

Since they lie in the THz range, where the corresponding wavelengths (~100 μm) are large compared to the typical sizes of interstellar dust grains (~ 0.1 μm), these lines are totally unaffected by the interstellar extinction by grains that hinders optical and near infrared observations. With weak Einstein A coefficients, the lines are also not usually affected by self-absorption (they are *optically thin*) so that typical photons will

escape an emitting gas cloud. Furthermore, the energy levels that emit the lines lie within a few hundred K of the ground state, so that they are easily collisionally excited by e^{-1} , H, or H_2 impacts in many astrophysical environments. The combination makes these THz lines important coolants for many phases of the ISM and excellent probes of the physical conditions of the gas clouds and probes of the sources of heat, be it the radiation fields from nearby stars or AGN, cosmic rays, X-rays or interstellar shocks.

| Table 1: Selected THz Spectral Lines | | | | | | |
|--------------------------------------|-------------------------|-------------------|-----------------------------|-------------|-----------------------|---|
| Species | Trans. | E.P. ¹ | λ (μm) | ν (GHz) | A (s^{-1}) | n_{crit} (cm^{-3}) ² |
| O^0 | $^3P_1 - ^3P_2$ | 228 | 63.18 | 4745 | 9.0×10^{-5} | $4.7 \times 10^{5(*)}$ |
| | $^3P_0 - ^3P_1$ | 329 | 145.53 | 2060 | 1.7×10^{-5} | $9.4 \times 10^{4(*)}$ |
| O^{++} | $^3P_2 - ^3P_1$ | 440 | 51.82 | 5786 | 9.8×10^{-5} | 3.6×10^3 |
| | $^3P_1 - ^3P_0$ | 163 | 88.36 | 3393 | 2.6×10^{-5} | 510 |
| C^+ | $^2P_{3/2} - ^2P_{1/2}$ | 91 | 157.74 | 1901 | 2.1×10^{-6} | $2.8 \times 10^{3(*)}$ 50 |
| N^+ | $^3P_2 - ^3P_1$ | 188 | 121.90 | 2459 | 7.5×10^{-6} | 310 |
| | $^3P_1 - ^3P_0$ | 70 | 205.18 | 1461 | 2.1×10^{-6} | 48 |
| N^{++} | $^2P_{3/2} - ^2P_{1/2}$ | 251 | 57.32 | 5230 | 4.8×10^{-5} | 2.1×10^3 |
| C^0 | $^3P_2 - ^3P_1$ | 63 | 370.42 | 809.3 | 2.7×10^{-7} | 1.2×10^3 |
| | $^3P_1 - ^3P_0$ | 24 | 609.14 | 492.2 | 7.9×10^{-8} | 4.7×10^2 |
| ^{12}CO | J=13-12 | 503 | 200.23 | 1497 | 2.2×10^{-4} | 2.5×10^6 |
| | J=11-10 | 365 | 236.60 | 1267 | 1.3×10^{-4} | 1.4×10^6 |
| | J=9-8 | 249 | 289.12 | 1037 | 7.3×10^{-5} | 8.4×10^5 |
| | J=7-6 | 155 | 371.65 | 806.7 | 3.4×10^{-5} | 3.9×10^5 |
| ^{13}CO | J=6-5 | 116 | 433.56 | 691.5 | 2.1×10^{-5} | 2.6×10^5 |
| | J=12-11 | 413 | 226.89 | 1321 | 1.5×10^{-4} | 1.6×10^6 |
| | J=8-7 | 190 | 340.17 | 881.3 | 4.5×10^{-5} | 1.7×10^5 |
| | J=6-5 | 111 | 453.48 | 661.1 | 1.9×10^{-5} | 2.3×10^5 |

¹Excitation potential, energy (K) of upper level above ground.
²Collision partner for atoms are electrons except those marked with a (*). These have collision partners of H and H_2 (100 K).

B. Ionized Gas Lines

It takes 13.6 eV photons to ionize hydrogen, so species that require more than 13.6 eV photons to form will be found exclusively within HII regions (O^{++} , N^+ , N^{++}), and those with ionization potentials less than 13.6 eV (O, C) will be found exclusively in neutral gas clouds. C^+ takes only 11.3 eV photons to form, but 24.4 eV to further ionize so that it is found both in neutral and ionized gas clouds. Fine-structure lines are excellent probes of gas density. Within a species, two fine-structure lines will have different A coefficients, hence different critical densities (n_{crit}) for thermalization of the emitting levels¹. In the low density limit ($n \ll n_{\text{crit}}$), every collisional excitation leads to the emission of a photon, so that the line ratio is constant (Fig. 1). In the high density limit ($n \gg n_{\text{crit}}$), the levels populations are thermalized, and given by the Boltzman formula therefore yielding a second constant line ratio. Between the low and high density limits the ratios vary

¹ The critical density for thermalization of an emitting level is defined as the density at which collisional de-excitations of the level equal radiative de-excitations.

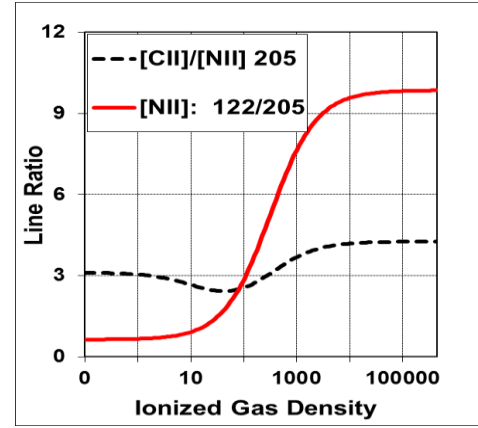


Fig. 1. Ratio of the [NII] 122 μm to 205 μm fine-structure lines as a function of gas density (solid line). The line ratio is a sensitive probe of gas density for HII regions with electron densities between 20 and 2000 cm^{-3} . Also shown is the ratio of the [CII] 158 μm /[NII] 205 μm lines as a function of gas density. This line ratio can be used to discern the fraction of the observed [CII] line that arises from ionized gas regions [1].

strongly with gas density as first one, and then the other emitting level is thermalized. For the lines that arise in ionized gas regions, the level excitation potentials (energy above ground state) are much less than the ionized gas temperatures (~ 8000 K), so that level excitation is very insensitive to gas temperature. However, neutral oxygen and carbon are found in neutral gas regions where gas temperatures are typically between 50 and 1000 K. Therefore, their line ratios are sensitive to gas temperature. The critical density of the carbon lines are relatively modest so that the levels are typically thermalized at the densities found in interstellar gas clouds. As such, the [CI] line ratio has proven to be a good temperature probe, and the lines trace gas column density, hence mass.

The THz frequency fine-structure lines are also excellent probes of the hardness of the ambient interstellar radiation fields. The vast majority ($\sim 90\%$) of stars in galaxies like the Milky Way are on the main sequence (MS) where they are fusing hydrogen into helium in their cores. Within the main sequence, stellar luminosities, L_{MS} are strongly dependent on stellar mass, M : $L_{\text{MS}} \sim M^3$ to 3.5 , so that the most massive stars dominate the interstellar radiation fields. Due to this steep dependence of L on M, the most massive stars also have the shortest lifetimes on the main sequence, $\tau_{\text{MS}} \sim M^{-2.5}$. More massive MS stars also have much higher effective surface temperatures, T_{eff} so they put out much harder radiation fields. Therefore, presuming a stellar photospheric origin, a harder ambient radiation field indicates more massive stars on the main sequence, hence a younger stellar population. The fine-structure lines trace the radiation field hardness, hence the *age of the starburst*. It takes 14.5 eV photons to form N^+ (equivalent $T_{\text{eff}} \sim 33,000$ K, or a B0 star), and 29.6 eV photons to form N^{++} ($T_{\text{eff}} \sim 39,000$ K or an O8 star), so that the [NII]/[NIII] line ratios are strongly indicative of the hardness of the ambient interstellar radiation field (Fig. 2). With an ionization potential of 35 eV, O^{++} takes even harder UV photons to form than N^{++} . Therefore, the [OIII]/[NII] line

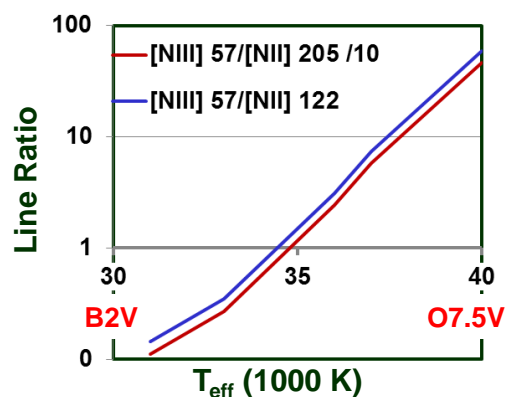


Fig. 2. Ratio of the [NIII] 57 μm to [NII] 122 μm and 205 μm lines as a function of effective temperature of the ionizing star. This line ratio is a very strong diagnostic of the most massive star on the main sequence with line ratios that grow by factors of 1000 when the stellar type changes from B2 to O7.5 stars (based on [2]).

ratios are even stronger indicators of T_{eff} . The [OII] 88/[NII] 122 μm line is especially useful since the levels that emit these lines have similar critical densities, so that the resulting line ratio is very insensitive to density as well (Fig. 3).

C. Neutral Gas Lines

In astrophysical environments, as one moves away from the source of ionizing photons there is a transition from regions where hydrogen is fully ionized (the HII region) to the neutral gas clouds beyond. While HII regions and neutral gas clouds have size-scales of the order parsecs (3.1×10^{18} cm), the transition between the two is fairly abrupt. It is roughly given by the mean free path of a photon that is capable of ionizing H, or ~ 0.01 pc for typical interstellar gas densities. Photons with energies less than 13.6 eV escape the HII region and penetrate the neutral gas clouds beyond where they can ionize elements with ionization potentials less than 13.6 eV (e.g. C), and photodissociate molecules with dissociation energies less than 13.6 eV (e.g. CO, H₂, H₂O) forming a photodissociation region (PDR) (see [4]). The depth of the PDR into the cloud can be defined as the depth of penetration of photons capable

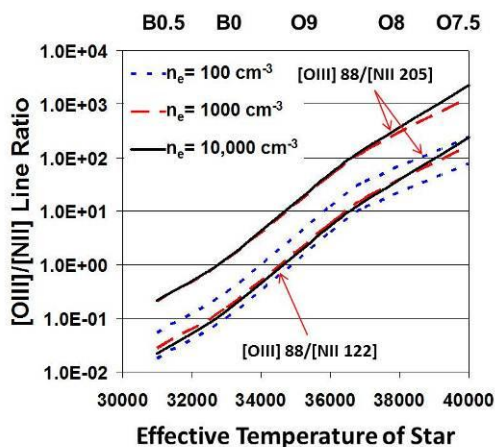


Fig. 3. Ratio of the [OIII] 88 μm to [NII] 122 μm and 205 μm lines for three ionized gas densities as a function of T_{eff} of the ionizing star. This ratio is extremely sensitive to T_{eff} and very insensitive to gas density, especially the [OIII] 88 to/[NII] 122 μm ratio [3], based on [2].

of ionizing carbon. This depth is typically determined by the extinction of these photons by dust, and is roughly given by a visual extinction, $A_V \sim 3$, which corresponds to a hydrogen column density of 6×10^{21} cm^{-2} , or ~ 1 pc for a typical gas density of 2000 cm^{-3} . Within the PDR gas is heated by the photo-electric (PE) effect – whereby hot electrons are ejected from grains by FUV photons ($6 < h\nu < 13.6$ eV) and transfer their excess kinetic energy to the gas before recombining with grains. The efficiency of this heating mechanism depends on the grain charge. If the charge gets larger, more of the next photon's energy is expended in freeing the electron from the positive potential of the grain, leaving less excess kinetic energy for heating the gas, thereby lowering gas heating efficiency. Therefore, the gas heating efficiency goes down as the ambient radiation field strength goes up. However, this can be mitigated by larger gas densities that will increase electron-grain recombination rates, lowering the grain charge. The PE heating efficiency is typically 0.1 to 1%. The rest of the FUV radiation field goes into heating the grains which then emit in the THz continuum. The gas is primarily cooled through collisional excitation of the ground state fine-structure levels of C⁺ and O and subsequent emission in their THz lines. To a lesser extent, the neutral carbon fine-structure lines and the mid-J CO rotational lines are also important coolants for these PDRs. The combination of the [CII] (158 μm), and [OI] (63 and 146 μm) fine-structure lines enables unique determination of PDR gas temperature and density. Since the combined luminosity of these lines gives the gas heating, and the luminosity of the THz dust continuum radiation is directly proportional to the luminosity of the ambient radiation fields, the ratio of the two yields the PE heating efficiency, hence strength of the ambient FUV radiation fields. It can be shown (see [5-8]) that for most astrophysical environments that apply over kilo-parsec (kpc) scales in galaxies, the [CII]/far-IR continuum ratio in of itself is an excellent indicator of the FUV field strength and can be used as an indicator of the physical size of the astrophysical source.

A challenge with the [CII] line is that it arises from both ionized and neutral gas regions, so that its diagnostic potential can be problematic. Fortunately, the [NII] 205 μm line has the same critical density for excitation by electron impacts as [CII] so that the [CII]/[NII] 205 μm line ratio from HII regions is only a function of the assumed N⁺/C⁺ abundances within the HII region (see Fig. 1). Therefore, the 205 μm [NII] line strength yields the fraction of the observed [CII] emission that arises from ionized gas ([1]), and the [CII]/[NII] combination constrains the physical conditions and cooling of two major components (ionized and PDR) of the ISM.

D. The Importance of the THz Fine-Structure Lines

The THz fine-structure lines are bright. For star forming galaxies, the brightest of these lines is typically the 158 μm [CII] line which can be the brightest single spectral line from the galaxy as a whole, and typically accounts for between 0.1 and 1% of far-IR luminosity of the system ([6]). From the Milky Way galaxy this amounts to 70 million solar

luminosities (L_{\odot}) [9,10], for nearby ultraluminous infrared galaxies, those with far-IR luminosities exceeding $10^{12} L_{\odot}$ the [CII] line can have luminosities of $10^9 L_{\odot}$ ([11]), while in distant hyper-luminous galaxy ($L_{\text{far-IR}} > 10^{18} L_{\odot}$), ten billion solar luminosities of power often emerges in this single line ([8,12])! Other lines, in particular [OI] 63 μm and the [OIII] lines often are nearly equal in luminosity to the [CII] line with the [NIII], [NII], and [OI] 146 μm lines only a factor of 5 to 10 fainter [13]. These lines are bright because they are cooling lines. Cooling lines are important as an interstellar cloud must cool to enable it to collapse to form the next generation of stars. It is the extinction free nature, and powerful diagnostic utility of these lines, together with their intrinsic brightness that makes their study so compelling, even from the most distant sources in the Universe.

E. Molecular Lines

The brightest of the molecular lines in the THz regime are the mid-J rotational lines of CO. These lines probe the warm, dense gas immediately interior to the atomic regions in PDRs and can be quite strong in molecular shocks. The run of line intensity with J constrains the physical conditions of the emitting gas. Several of the rotational lines can be optically thick, so that radiative transfer effects must be considered. Typically radiative transfer is handled within a “large-velocity gradient” model. These models have degeneracies between optical depth effects, and those of gas excitation (density and temperature), so that it is important to measure low optical depth isotopologues of CO, most commonly ^{13}CO transitions to break these degeneracies. The absolute strength of the lines compared to the THz continuum and fine-structure lines can reveal the source of heat. For example, strong CO lines and relatively weak THz lines indicates non-PDR origins for the CO emission: the gas may be heated by super-sonic shocks, cosmic rays or X-rays [14-17].

F. The Importance of the THz Molecular Lines

Stars form from dense molecular clouds. To enable sustained collapse, clouds must cool through THz line radiation. Studies have shown that up to half of the molecular ISM in starburst galaxies is warm and dense [14-15],[17-19], so that it is important to study this gas through its mid-CO cooling line emission to understand the interplay between star formation and the natal molecular clouds. For example, for some starburst nuclei, supernovae blasts might compress the ISM leading to the formation of the next generation of stars so that the starburst is self-sustaining, while for others far-UV and cosmic ray heating, and molecular flows may energize or disrupt the ISM making the starburst self-limiting [15]. Notice that since the low J ($J < 4$) lines have smaller excitation requirements, their line ratios are relatively insensitive to the physical parameters of the gas.

III. ASTROPHYSICAL OBSERVATIONS

A. A Short History

The far-IR fine-structure lines discussed above were

recognized as important astrophysical coolants long before their detection, cf. [20-22], but their astrophysical detection was hindered by (1) the strong telluric absorption from water vapor which makes detection of all but the [CI] lines nearly impossible from ground based telescopes, (2) the uncertain transition frequencies of the major lines, and (3) the still emerging state of detector technology at this time. With the advent of NASA’s airborne observatories including the 12 inch telescope on the Lear Jet Observatory and 36 inch telescope on the Kuiper Airborne Observatory (KAO) in the early 1970’s, which enabled observations above 99.8% of the atmospheric water vapor, most of the lines were rapidly detected including the [OIII], [OI], and [CII] lines by Martin Harwit’s group at Cornell University using a grating spectrometer on the Lear Jet [23-27], the [NIII] line using a Michelson Fourier transform spectrometer (FTS) on the KAO [28], the [NII] lines with the FIRAS FTS on COBE [10], and by Edwin Erickson’s group at NASA Ames using a grating spectrometer on the KAO [29], and the [CI] lines using heterodyne receivers on the KAO [30] (492 GHz), and from the ground [31], (809 GHz). At about the same time, several of these lines were also detected by balloon-borne experiments including mapping of the galaxy in [CII] with an Fabry-Perot interferometer (FPI) [32], and the Orion Nebula in several lines with a Michelson interferometer [33]. These galactic observations were soon followed up by extragalactic FPI work in the Townes/Genzel group at UC Berkeley and at MPE Garching (e.g. [6],[34-36]) and within Edwin Erickson’s group at NASA Ames ([37-39]). Nearly all of these observations were obtained with direct detection spectrometers (gratings, FTS, and FPI) that utilized Ga:Ga photoconductors as detective devices. The exceptions were the [CI] lines that were first detected using heterodyne techniques using hot electron bolometers ([30]) or Schottky-diodes as mixers ([31]).

The first THz molecular lines detected from external galaxies were the bright mid-J CO rotational lines. These lines were first detected using heterodyne receivers from galactic sources. The first extra-galactic detection of a mid-J line, the CO(6-5) line at 690 GHz was detected from the nearby starburst nuclei of NGC 253, M82, and IC 342 using a Schottky-diode based receiver [18]. The CO(7-6) (809 GHz) line was first detected and mapped from an extragalactic source in the local Universe, NGC 253 using a direct detection spectrometer, SPIFI ([14] see below). (The line had previously been detected from high redshift sources, e.g. [40]). The first extra-galactic mid-J line of ^{13}CO detected was the 6-5 line, also detected from NGC 253, using the ZEUS grating spectrometer, ([15] see below).

In 1996, ESA launched the Infrared Space Observatory, a 60 cm cooled telescope in Earth orbit that contained both a FPI and a grating spectrometer for THz spectroscopy. The space-based platform opened an un-obscured view of these lines, albeit at wavelengths short-ward of the long wavelength cut-off of stressed Ge:Ga photoconductors, near 200 μm . An example of ISO based fine-structure line science is outlined

enveloping intense regions of star formation. At higher J , the spectrum flattens out with near uniform intensity. This flattening of intensity at the highest J is predicted for an X-ray dominated region (XDR) – a molecular region whose primary source of heat is intense X-ray illumination [49]. The XDR is very likely associated with the “confining torus” of molecular gas thought to envelope the AGN, and the source of X-ray radiation is most likely the AGN itself. The strong OH^+ and H_2O^+ line emission strongly support the XDR heating mechanism. This is the first direct detection of the hot molecular torus long thought to circulate about the supermassive black holes that power AGN.

D. Recent Results: The Early Universe

The COBE satellite discovered that integrated over the history of the universe, half of the photospheric emission from stars is absorbed by dust in their nascent molecular clouds [50-51]. The heated dust then reradiates its energy in the FIR, with power typically peaking in a broad band centered near 60-100 μm . Much of this cosmic infrared background was subsequently resolved by large and sensitive telescopes into several classes of luminous star forming galaxies that emit primarily in the FIR to submm bands ($\sim 30 \mu\text{m} < \lambda < 1 \text{mm}$, S3), most of which lie at redshifts beyond 1 or look-back times beyond 7.7 Giga years (Gyr) [52], and indeed, the peak of star formation activity per unit co-moving volume occurred between redshifts 1 and 3 (2 to 6 Gyr after the Big Bang) at a rate 10-20 times the current value [53]. Continuum surveys are the means of discovery for these distant galaxies, but spectroscopy is the only method for unraveling the physics of the interstellar medium and the properties of the stellar populations. Since these systems are highly obscured, FIR/submm spectroscopy is key to these studies.

The [CI] lines were the first THz fine-structure line detected at high redshift, detected from the lensed Cloverleaf quasar at $z = 2.56$ [40],[54]. These lines, together with CO lines, were used to show that the molecular disk is surprisingly modest mass within this system. The brightest THz fine-structure line, the [CII] line was first observed at high redshift from the very high redshift ($z=6.42$) quasar, SDSS J1148+5251 [55]. The line was subsequently detected in two other high z ($z > 4.4$) quasar dominated systems, each of which show a low $L_{[\text{CII}]} / L_{\text{FIR}}$ ratio reminiscent of that found in some ULIRG galaxies in the local Universe [56-57]. In local ULIRGs this low ratio is interpreted as either intense FUV fields lowering the $L_{[\text{CII}]} / L_{\text{FIR}}$ luminosity ratio since [CII] line saturates, while continuum does not, or due to presence of additional non-PDR origin for the FIR continuum [11].

The first detection of a high z [CII] line from the $z = 1-3$ epoch of peak star formation in the Universe, and also the first detection of [CII] from a high z galaxy not association with a quasar was made from MIPS J1428 at $z = 1.33$ using the ZEUS spectrometer [7]. Here the $L_{[\text{CII}]} / L_{\text{FIR}}$ ratio is large, comparable to nearby starburst galaxies, and when combined with the CO(1-0) line, indicates the ISM in MIPS J1428 contains molecular clouds with similar gas densities and exposed to

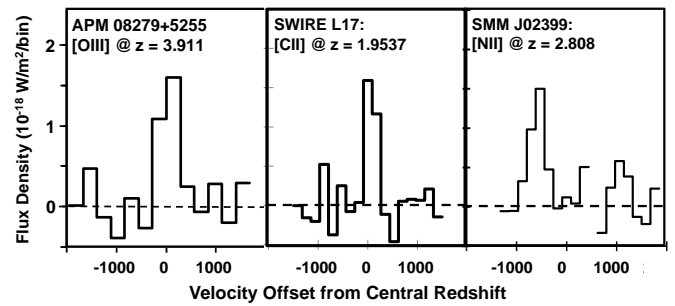


Fig. 6. ZEUS/CSO detections of [OIII] 88 μm , [CII] 158 μm , and [NII] 122 μm fine-structure lines from high redshift systems [58], [6], [3].

similar radiation fields as those found in M82. But, since MIPS J1428 is forming stars at the rate of 1800/year compared to ~ 5 /year for M82, the starburst must be enormous in this source, with an estimated diameter of 3-8 kpc, essentially involving the entire galaxy. This first detection was followed up by a [CII] survey containing 12 detections of galaxies in the $z \sim 1$ to 2 interval in the [CII] line quadrupling the numbers of systems then reported [7] (Fig. 6). Within this survey, those systems dominated energetically by star formation (SBD) have a $L_{[\text{CII}]} / L_{\text{FIR}}$ luminosity ratio eight times that of those dominated by AGN activity, so this ratio picks out systems dominated by AGN. As for MIPS J1428, the SBD systems have starbursts similar in intensity to that of M82, but the starbursts extend over kiloparsec scales – very unlike the confined (few hundred pc scales) found for starbursts in local starburst or ULIRG galaxies. Essentially the entire galaxy is erupting in a super-massive starburst. Clearly the mode of star formation is quite different at early times than it is today.

The THz fine-structure lines of [OIII] are now reported from high z systems. The 88 μm line was detected first from two AGN/starburst systems at high redshifts using the ZEUS spectrometer on the CSO [58] (Fig. 6). For SMM J02399 ($z=2.8$), the line was used together with the THz continuum to estimate the age of the starburst and most massive star on the main sequence. For APM 08279 ($z=3.9$) it was found that the line could arise from either the narrow line region of the AGN, or from a starburst headed by O7.5 stars. Very recently, the [NII] 122 μm line was detected for the first time at high z , from SMM J02399 and the Cloverleaf [3] (Fig. 6). The [OIII]/[NII] line ratio tightly constrains the radiation field (Fig. 3), and it is found that SMM J02399’s current stellar population is dominated by O9.5 stars, indicating a 3 million year old starburst.

The [OIII] 52 μm line was detected by PACS on the HSO from MIPS J1428 ($z=1.3$), and IRAS F10214 ($z=2.28$) [59]. The line is compared with the THz continuum to show that the former source is similar to local starburst galaxies, while the latter is similar to local ULIRGs. The first high z detection of [OI] 63 μm (from MIPS J1428) was also reported in this paper, confirming the [CII] based conclusions [6].

IV. DIRECT DETECTION SPECTROSCOPY

It is very challenging to achieve very high spectral resolving powers (RP) with direct detection systems in the THz regime.

For instance, in a single pass configuration, a grating spectrometer with $RP \equiv v/\Delta v \sim 10^5$ at 1 THz ($\lambda=300 \mu\text{m}$) needs an effective delay path, $d \sim 10^5 \cdot 300 \mu\text{m}/2 = 15$ meters. Even within a multiple pass system, like a Fabry-Perot with finesse ~ 30 the path is still a challenging 50 cm. Therefore, the only reasonable way to achieve these very high RP at THz frequencies is with heterodyne detection techniques. However, for the modest RP required for extragalactic spectroscopy (1000), delay paths are modest (~ 15 cm) so that direct detection spectrometers are straightforward to construct.

In an incoherent, or direct detection spectrometer the energy of the incoming photon is used to create a signal either by heating a detector (as in a bolometer) or in causing an electron to make a quantum transition from a valence to conduction band in a semi-conductor (as in a photoconductor). A coherent, or indirect detection system relies on the wave nature of light. The advantage of a coherent receivers is that the spectral RP can be made extremely high, and the preservation of phase makes them easy use for aperture synthesis. The systems we compare to in the THz band are heterodyne receivers, where the THz wave from the astronomical source is beat against a local oscillator to mix the signal down to gigahertz frequencies where it is efficiently detected in a square law device such as an SIS mixer. Coherent detection preserves photon phase and requires signal amplification before detection. This results in an uncertainty in photon occupation number of one photon/Hz/sec. This “quantum noise” when expressed in terms of temperature of a radiation field that produces the same noise, is given by $T_{\text{QN}} = hv/k = 48$ (v/THz) K, where h and k are Planck’s and Boltzman’s constants respectively. The quantum noise is unavoidable, and provides a sensitivity floor for the receiver noise temperature of a heterodyne receiver: $T_{\text{rec}} > T_{\text{QN}}$. The best modern receivers come within a factor of ~ 4 of the QN limit at low frequencies (e.g. T_{rec} (DSB) ~ 50 K @ 345 GHz [60], and 75 K at 670 GHz [61]), and within a factor of 15-25 of the QN limit at frequencies above 1.2 THz (e.g. T_{rec} (DSB) ~ 1000 K @ 1.3 THz [62], and ~ 3000 K at 2.55 THz [63]).

Arguably, one of the most exciting applications of moderate RP THz spectroscopy today is the detection of the THz fine-structure lines from high redshift galaxies. This entails maximizing point source sensitivity over broad bandwidths. Here we compare the relative utility of coherent and incoherent receivers for this work, and demonstrate a compelling case for direct detection at THz frequencies. In terms of the receiver temperature in the presence of background with equivalent noise temperature T_{bkg} , the rms noise temperature at the front end of a coherent receiver, ΔT_{FE} in a bandwidth Δv , in integration time, Δt is given by:

$$\Delta T_{\text{FE}} = a \cdot \frac{(T_{\text{bkg}} + T_{\text{rec}})}{(\Delta v \cdot \Delta t)^{1/2}}$$

where $a=1$ or 2 depending on whether the receiver is configured for single-side-band or double-side-band detection. Clearly if the background is large, and the receiver temperature is small, the effect of the receiver temperature on

the overall sensitivity is small. This would be the case for a receiver at 100 GHz, with noise temperature $\sim 4 \cdot T_{\text{QN}} \sim 19$ K, operating from the ground where the combined emissivity of the telescope and the sky might be 15%, i.e. $T_{\text{bkg}} = 0.15 \cdot 300$ K = 45 K. However, in space, where T_{bkg} can approach 2.73 K, and at THz frequencies, where 4 to $15 \cdot T_{\text{QN}} = 190$ to 720 K, the receiver noise can easily dominate that of the background.

In principle, the sensitivity of a direct detection system is only limited by the statistics of the photon arrival rates. For the case of low photon occupancy ($hv/kT \gg 1$), which applies in the optical band, the noise follows a Poisson distribution, so that the detection of N photons, has an associated noise, $N^{1/2}$. However, in the THz regime, $hv/kT \sim 1$, so that the effects of photon bunching must be included. The noise equivalent flux, NEF_{inc} [Watts/m²/Hz^{-1/2}], of a background limited performance (BLIP) spectrometer with cold transmission τ (emissivity 0), operating on a telescope with collecting area, A , efficiency η_{tel} , at temperature T , looking through a sky with transparency η_{sky} , at temperature T , using spectrometer pixels that have point source coupling η_{pixel} , and detective quantum efficiency (DQE) η , is given by [64]:

$$NEF_{\text{inc}} = \frac{2h\nu}{(A\eta\tau \cdot \eta_{\text{sky}}\eta_{\text{tel}}\eta_{\text{pixel}})} \left(\frac{2A\Omega}{\Delta t \cdot \lambda^2} \Delta v \cdot c_1(1+c_1) \right)^{1/2}$$

where Δt , and Δv are as before, Ω is the beam solid angle, and $c_1 = \varepsilon \cdot \eta \cdot \tau \cdot \bar{n}$ is the product of the warm emissivity ε , η , the spectrometer cold transmission τ , and the mode occupation number, $\bar{n} = 1/(\exp(hv/kT)-1)$. The effective emissivity of the background ε , is roughly given by $\varepsilon \sim (1-\eta_{\text{sky}}) \cdot \eta_{\text{tel}} + (1-\eta_{\text{tel}})$. The first factor of 2 in this expression arises due to chopping losses of the telescope, while the second factor of 2 is due to the detection of both polarizations of light. The equivalent expression for the heterodyne system is:

$$NEF_{\text{coh}} = \frac{2 \cdot 2k \cdot \Delta T_{\text{FE}}}{(\lambda^2 \cdot \eta_{\text{sky}}\eta_{\text{tel}}\eta_{\text{taper}})} \Delta v \cdot \Omega$$

where η_{taper} is the effective fraction of the power in the main beam that couples to a point source due to the edge taper of the beam, and the other parameters are as above. Equating the two expressions and using (1), we have:

$$T_{\text{bkd}} + T_{\text{rec}} = \frac{h\nu}{(ak\eta\tau)} \left(\frac{\eta_{\text{taper}}}{\eta_{\text{pixel}}} \right) \cdot \left(\frac{2c_1 \cdot (1+c_1)}{1.69\pi} \right)^{1/2}$$

The factor of 1.69π arises since we assume diffraction limited, Gaussian beams, where $\theta = 1.22\lambda/D$, and $\Omega = \pi \cdot (\theta/2)^2 / \ln(2)$. Here θ is the beam full-width-at-half maximum, and D is the diameter of the telescope primary mirror. We use the ZEUS and ZEUS-2 spectrometers as an example (see below). These spectrometers have $\tau \sim 35\%$, bolometers with $\eta \sim 0.9$, and $\eta_{\text{pixel}} \sim 0.7$. Referring to a single sideband receiver ($a=1$) then for BLIP at 850 GHz at an excellent ground based site ($\eta_{\text{sky}} \sim 58\%$, $T=260$ K) and assuming $\eta_{\text{taper}}=1$, a coherent single-side-band receiver would need to have a noise temperature of 16 K to be equivalent to a background limited grating spectrometer for point source detection. The ZEUS spectrometer achieves roughly this value in practice [65]. With modern bolometers, it

is straight-forward to achieve BLIP in the THz bands for RPs $\sim 10,000$, from the ground and airborne facilities so that direct detection systems are the spectrometers of choice for detecting broad spectral lines.

V. DIRECT DETECTION THZ SPECTROMETERS IN USE TODAY

In this section we describe four current state-of-the-art spectrometers in use at THz frequencies today, including a Fabry-Perot interferometer (SPIFI), a long-slit grating spectrometer (ZEUS), an image slicing grating spectrometer (PACS), and a Fourier transform spectrometer (SPIRE). Each of these spectrometers performs close to the fundamental limits, and due to their unique architecture, has a unique niche of scientific excellence.

A. Comparisons Between Direct Detection Spectrometers

The choice of direct detection spectrometer strongly depends on the science at hand. An FPI or an FTS have much larger luminosity-resolution products at a given R than grating spectrometers that require entrance and exit slits [66]. The FPI/FTS are also readily adapted to imaging spectroscopy so that within limits given by the angular divergence of rays in the beam, large, 2-dimensional focal plane arrays of detectors are easily implemented into these spectrometers creating *spectroscopic imagers*. For detection of a single isolated line over broad regions, the FPI will win over an FTS since, in a BLIP environment, the narrow band of the FPI will deliver much higher sensitivity than the broadband FTS (below). If, however, one wishes to detect many lines over a very broad range, this sensitivity advantage of the FPI becomes small, and an FTS becomes competitive. However, in terms of raw sensitivity for point source detection, a spectrally multiplexed grating spectrometer is the instrument of choice.

Let us compare a monochromator (FPI or grating spectrometer) to an FTS of the same RP (see also [67]). We desire to obtain a spectrum with overall bandwidth B, split into N spectral resolution elements, $\Delta\nu$: $B=N\cdot\Delta\nu$. Suppose both instruments have BLIP with noise per resolution element in the monochromator given by σ_{mono} . The FTS takes in the entire bandwidth, B at the same time, encoding the power of all spectral elements into each step of the interferogram. Since the FTS detector therefore sees the full bandwidth, the noise per unit time is larger than that of the monochromator by $\sigma_{\text{FTS}}=(B/\Delta\nu)^{1/2}\cdot\sigma_{\text{mono}}=N^{1/2}\cdot\sigma_{\text{mono}}$. However, if the monochromator is an FPI, one has to scan N resolution elements to deliver the equivalent spectrum as the FTS does in a single interferogram. Therefore, the total time to deliver the same spectrum is N times longer, so that N interferograms are obtained in the same time as one FPI scan. In this case, then the noise of the FTS spectrum goes down by $N^{1/2}$, and the two systems are equal.² However, a spectrally multiplexed grating

² Note that we have ignored the factor of 2 encoding losses of the FTS in this argument. This loss is because the average signal of the interferogram is half the white light signal. However, the FPI will likely have smaller transmission than the FTS due to etalon absorption or the extra filtration needed, so this encoding loss is at least in part cancelled in the comparison.

spectrometer can have N detectors in the dispersion direction, so that it need not spectrally scan. For this case then, the grating spectrometer is more sensitive than the FTS by $N^{1/2}$. If, however, the detectors are not background limited – i.e. the noise is independent of bandwidth – the sensitivities become equal again. In this case, the FTS becomes a very interesting choice since it delivers the same N resolution element spectrum as the grating spectrometer, but with just one detector, not N so that it provides a much more effective use of what is often the rarest commodity, the numbers of pixels.

B. SPIFI – A Bolometer-based Imaging Fabry-Perot

The South Pole Imaging Fabry-Perot Interferometer (SPIFI) is the first direct detection imaging spectrometer for use in the submillimeter bands [64], [68-69]. Unlike previous THz astronomical spectrometers that used either heterodyne techniques, or photoconductors, SPIFI employed bolometers as detectors for the first time. Bolometers have several clear advantages over photoconductors: (1) Ge:Ga photoconductors have DQE's of the order 3 to 26% [70-71]. In contrast, it is easy to design a bolometer with 50% DQE over very large bandwidths, or by using tuned backshorts, > 90% DQE over broad ($\lambda/\Delta\lambda \sim 3$) bandwidths [72]. (2) Photoconductors detect photons by discretely generating photoelectrons (or holes). The generation and recombination of these photoelectrons generates shot noise, commonly termed generation recombination (GR) noise. Bolometers are thermal devices so that they do not suffer from GR noise. Therefore, for a given DQE, a bolometer will be twice as sensitive as a photoconductor. (3) Bolometers are inherently broad-band with nearly constant DQE over this band. Unlike photoconductors, bolometers do not have long wavelength cut-offs due to minimum energy requirements for promotion of electrons from the conduction to valence bands, or poor short-wavelength performance due to strong frequency dependence of ionization cross sections. The photoconductor with the longest wavelength cut-off is stressed Ge:Ga, which has a long-wavelength cut-off near 210 μm or 1.43 THz. The combined sensitivity advantage of bolometers as detectors over photoconductor goes as $\text{NEP} \propto \frac{1}{2} \cdot (\eta_{\text{PC}}/\eta_{\text{bol}})^{1/2}$, and can be large. As a working demonstration, under similar background conditions, SPIFI at 1.5 THz (200 μm) is a factor of ~ 10 more sensitive than background limited spectrometers that employed stressed Ge:Ga photoconductors as detective devices [1],[29],[70].

SPIFI is an imaging Fabry-Perot interferometer designed to work in the 850 GHz window available to the JCMT on Mauna Kea, and the 1.5 THz window available to the AST/RO telescope at South Pole [64],[68-69] (Fig. 7). SPIFI employs free-standing metal mesh mirrors in its FPI etalons, which typically deliver reflective finesse $\sim 25-60$, and transmissions $\sim 70-80\%$. SPIFI's RP is fully tunable through changing the order of the high-order FPI (HOFPI), and can be changed from ~ 500 to $\sim 10,000$ in a few minutes while the instrument is mounted on the telescope and operational. SPIFI achieves high spectral purity through the use of a low-order FPI (LOFPI) to

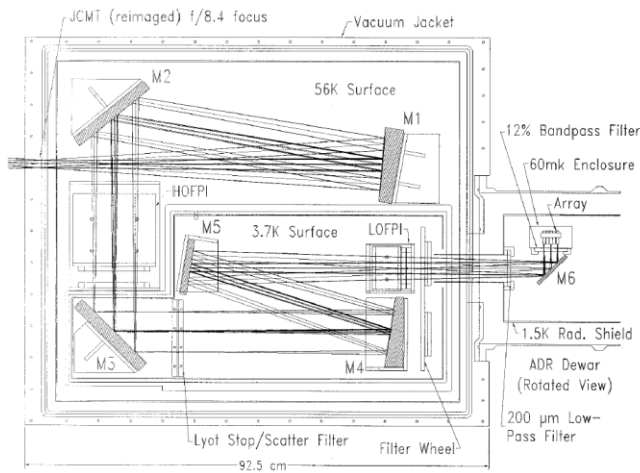


Fig. 7. Optical layout for SPIFI imaging Fabry-Perot [64].

select the desired order of the HOFPI, and a fixed bandpass filter to select the desired order of the LOPFI, enabling operation of the LOPFI in orders as high as 10 to 20. The detective devices in SPIFI are a 5×5 array of bolometers from Goddard Space Flight Center (GSFC), that are held at 60 mK in an adiabatic demagnetization refrigerator (ADR). SPIFI was deployed 6 times on the 15 m JCMT. Scientific highlights from these runs included the first detection and mapping of the CO(7-6) line from NGC 253, and the first large-scale map of the CO(7-6) and [CI] lines from the Galactic Center circumnuclear ring [14],[73-74].

SPIFI was also deployed on the 1.7 m AST/RO telescope at South Pole over the 2004 and 2005 Austral winter. The first season was cut short due to an unexpected rapid depletion of the liquid helium supply for the base, but the second season was quite successful. SPIFI was used in both the 859 GHz and 1.5 THz telluric windows. The highlight of the deployment was the detection and mapping of the [NII] 205 μm line from the Carina star formation region [1]. This was the first detection of this astrophysically important line from the ground, and its strength, when compared with the ISO [CII] and [NII] 122 μm mapping of the nebula demonstrates that the HII regions enveloping the Carina Nebula are low density ($n_e \sim 30 \text{ cm}^{-3}$), and that only 30% of the observed [CII] line radiation comes from the ionized medium (Fig. 1). Most (70%) of the [CII] radiation arises from PDRs.

SPIFI was close to background limited in both bands of operation: within a factor of 2 at 850 GHz [68], and within a factor of 1.4 at 1.5 THz [69]. The equivalent single-side-band receiver temperature was $T_{\text{rec}}(\text{SSB}) \sim 310 \text{ K}$ (40 K DSB) at 850 GHz, and $T_{\text{rec}}(\text{SSB}) \sim 610 \text{ K}$ (190 K DSB) at 1.5 THz, which compare quite favorably with the best heterodyne systems today [62],[75].

C. ZEUS/ZEUS-2: Bolometer Based Grating Spectrometers

ZEUS is an echelle grating spectrometer currently configured for operation in the 450 and 350 μm windows available on Mauna Kea [65]. ZEUS employs a 38 cm long R2 echelle grating blazed for 355 μm in 5th order (Fig. 8). As such, the ZEUS 5th and 4th orders of the echelle are well

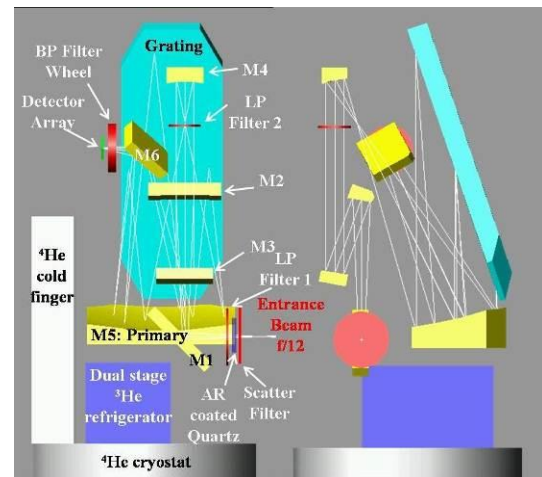


Fig. 8. Optical layout for ZEUS [65]. The grating is in near Littrow configuration.

matched to the 350, and 450 μm (860 and 670 GHz) telluric windows respectively (Fig. 9). The ZEUS grating is operated in near-Littrow mode, and delivers a RP ~ 1000 . This RP is near the diffraction limit, and the plate scale was selected so that most (~ 50 -80%) of the flux from a monochromatic point source is coupled into a single pixel. Since extra-galactic line widths are typically $\sim 300 \text{ km/sec}$, this choice of RP, and pixel size optimizes sensitivity for broad lines from point sources – e.g. distant galaxies. ZEUS employs a 1×32 pixel array of planar bolometers from GSFC with backshorts tuned to 400 μm resonance that delivers quantum efficiencies $>80\%$ over most of the operational band. ZEUS is run with order selecting band-pass filters immediately above the detector array: typically half the array operates in the 350 μm and half in the 450 μm windows. With each pixel corresponding to a resolution element, the instantaneous bandwidth of ZEUS is typically ~ 10 to 14 GHz. ZEUS is very close to background limited, coming within a factor of 1.2 and 1.3 of BLIP at 350 and 450 μm respectively. This performance figure corresponds to $T_{\text{rec}}(\text{SSB}) \sim 20$ and 35 K respectively in the centers of the 350 and 450 μm grating orders.

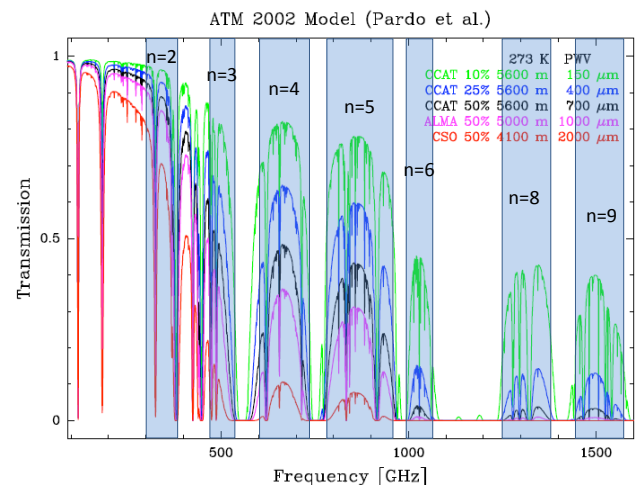


Fig. 9. Echelle orders (n) of ZEUS-2 superposed on telluric transmission plots for CCAT (best 10%, 25%, and 50% of nights), at the ALMA site (best 50% of nights), and at the CSO (best 50% of nights). CSO best 25% is similar to ALMA best 50%. ZEUS only accesses $n = 4$ and 5 orders.

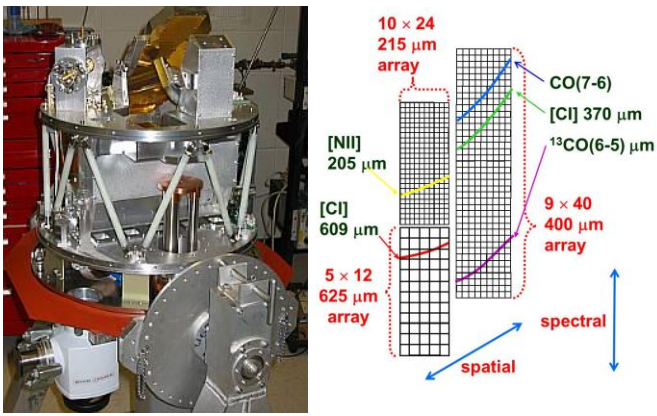


Fig. 10. (left) ZEUS-2 grating, optics, and cryogenics. (right). ZEUS-2 focal plane with grating tuned to simultaneous long-slit spectroscopy in the CO(7-6), $^{13}\text{CO}(6-5)$, [NII] and [CI] 370 and 609 μm lines [76].

ZEUS has been a regular on the 10.4 m CSO telescope since spring of 2006. Highlights of ZEUS/CSO include the detection of the $^{13}\text{CO}(6-5)$ line from the starburst nucleus of NGC 253 – the first detection of the $^{13}\text{CO}(6-5)$ line from an external galaxy, and the first detection of any ^{13}CO transition greater than $J=3-2$ from a source beyond the Magellanic clouds [15], and the several high redshift firsts mentioned above including (1) the first detection of the a THz fine-structure line of [OIII] at redshifts beyond 0.05 [58]; (2) the first detection of the [CII] line from the epoch of maximum star formation in the early Universe [7]; (4) the first survey of the [CII] line at high redshift [8]; and (5) the first detection of a THz [NII] line from a source at redshift beyond 0.05 [3]

ZEUS-2 is a multi-color, multi-beam version of ZEUS. The final instrument utilizes two TES sensed, SQUID multiplexed arrays from NIST [76]. The first is tuned with a $\lambda/4$ back-short to 400 μm , and consists of 280 pixels arranged in a 9 (spatial) \times 40 (spectral) format for use in the 300, 350 and 450 μm windows. The second consists of two sub-arrays. The first has 219 pixels arranged in a 10 (spatial) \times 24 (spectral) format, and is tuned with a $3\lambda/4$ backshort to 215 μm for use in the 200 and 230 μm telluric windows. The second sub-array consists of 56 pixels arranged in a 5 (spatial) \times 12 (spectral) format, and is tuned with a $\lambda/4$ backshort to 645 μm . The arrays should achieve DQE $>80\%$ in all bands. ZEUS-2 uses commercially available dual stage ADR and pulse tube cooling systems that not only eliminate the need for expendable cryogenics, but also lower the operating temperature of the cold head from 210 mK (with the ZEUS dual stage ^3He system) to 100 mK, ensuring greater margin on detector sensitivity.

ZEUS-2 is versatile. By using a filter wheel, the 9th through 2nd orders of the echelle are available for broad-band spectroscopy (Fig. 10). For low redshift, resolved objects ZEUS-2 delivers simultaneous spectroscopic imaging of five important astrophysical lines: the [NII] 205 μm , [CI] 609 and 370 μm , CO(7-6) and $^{13}\text{CO}(6-5)$ lines (Fig. 10). ZEUS-2 is nearly ready for first light on the CSO in the fall of 2011, and should deliver BLIP with equivalent receiver temperatures of

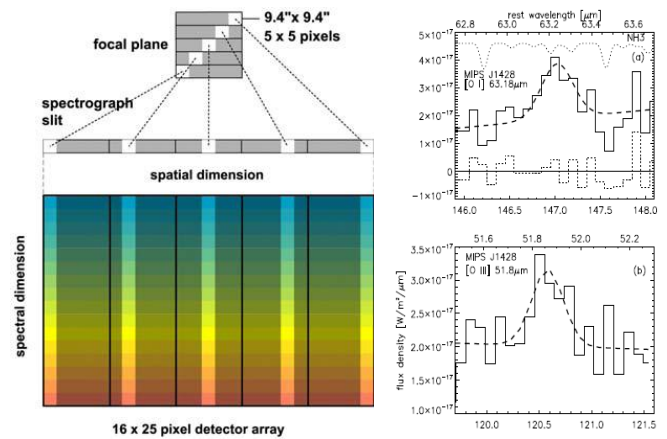


Fig.11. (left) Mapping the focal plane image onto a long slit within the PACS spectrometer. (right) [OI] 63 μm and [OIII] 52 μm fine-structure lines detected by PACS from the $z = 1.325$ starburst galaxy MIPS J142824 [59]

$T_{\text{rec}}(\text{SSB}) < 30 \text{ K}$ in all bands.

D. PACS

PACS is one of the three science instruments that operate on ESA's 3.5 m Herschel Space Observatory [77]. There are two modes to PACS, an imaging photometer mode, and an integral field spectrometer mode that delivers 16 pixel, Nyquist sampled $R \sim 1700$ spectra for each beam over a 5×5 beam ($47'' \times 47''$) field of view. The integral field is obtained by slicing the telescope image plane into 5 rows of 5 beams each with mirrors that direct and map each row independently onto a long grating entrance slit (Fig. 11). A long slit spectrometer is thereby transformed into a compact footprint imaging spectrometer. The detector arrays for PACS are two 16×25 pixel arrays of stressed and unstressed Ge:Ga photoconductors that are sensitive to photons between 105-210 and 57-105 μm respectively. The 30 cm long near Littrow mode grating is operated in 1st, 2nd and 3rd order covering 105-210, 72-105, and 55-72 μm respectively. The first order is separated from the 2nd and 3rd orders by a dichroic beam splitter and sent to the stressed Ge:Ga array, while the 2nd and 3rd orders are passed to the unstressed array. Along the short wavelength path a filter wheel enables selection of 2nd or 3rd orders. The detector arrays in PACS deliver peak DQE near 26% [71], resulting in 5σ , 1 hour detection limits of about $3\text{E}-18 \text{ W/m}^2$. These values are similar to those of ZEUS on CSO, so that there is a natural synergy between the two systems: redshift 1 to 2 galaxies detectable in [CII] with ZEUS are likely detectable in the [OI] 63 μm or [OIII] (52 or 88 μm) lines with PACS greatly enhancing the science yields of both systems.

The un-obscured views from space, combined with the great sensitivity of PACS has already lead to a number of exciting scientific results, including: (1) the first detection of the [OIII] 52 μm and [OI] 63 μm fine-structure lines from high redshift galaxies [59]; (2) the first survey of local starbursts, Seyfert (AGN), and IR luminous galaxies in the ensemble of far-IR fine-structure lines showing changes in the far-IR line to far-IR continuum ratio suggesting a shift to a higher efficiency mode of star formation in the most luminous systems [78]; and (3) the first evidence for massive molecular outflows in ULIRG

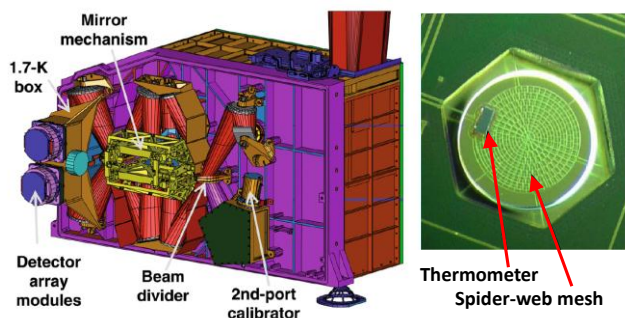


Fig. 12. (left) SPIRE interferometer optical path (right) close-up of a SPIRE spider-web bolometer showing the mesh architecture of the absorber, and the thermometer. The thermometer is $10 \times 100 \times 300 \mu\text{m}$ in size [80].

galaxies that may quench their star formation activity [79].

E. SPIRE

SPIRE is the second direct detection instrument on the HSO [80]. Like PACS, SPIRE contains both imaging photometer, and imaging spectrometer modules. The spectrometer is an FTS in a Mach-Zehnder configuration. The FTS contains twin interferometer arms modulated by the same scan mechanism, so that spectra are simultaneously obtained from two different bolometer arrays that are arranged to spatially overlap on the sky (Fig. 12). The first array covers the $194\text{--}313 \mu\text{m}$ band with 37 bolometers, and the second covers the $303\text{--}671 \mu\text{m}$ band with 19 bolometers. The bolometer arrays consist of discrete “spider-web” bolometers fed by single mode conical feed horns. These open architecture arrays deliver very low NEPs at the base temperature of 0.3 K delivered by the ^3He refrigerator plus exceptionally low susceptibility to cosmic ray hits [81]. The FTS resolution element is fully tunable from $2\text{--}0.04 \text{ cm}^{-1}$ (unapodized), so that the highest RP varies from 1300 and 370 from the shortest to longest wavelengths.

The unique SPIRE niche is very broad-band moderate resolution spectroscopy, underscored by the un-obscured vision of the HSO in space. SPIRE therefore has observed a variety of lines for the first time, or the first time from an external galaxy (Fig. 5). The broad bandwidth also enables simultaneous measurements of many rotational transitions of CO from galaxies, characterizing both PDRs and XDRs, and enabled the first detailed studies of water line emission from external galaxies [82]. SPIRE has performed far better than pre-launch expectations, delivering the requisite sensitivity to detect $z \sim 2.2$ redshifted fine-structure lines as well [83].

VI. FUTURE PROSPECTS

There are many new astrophysical discoveries being made right now using low resolution THz spectroscopy boosted by both developments in ground based instrumentation, and the spectacular success of Herschel in space. The future is even more exciting. The SOFIA facility is just now undergoing its first science flights, the enormously powerful ALMA facility has just released its call for first science proposals, and looming on the near horizon are the 25 m CCAT telescope, and the 3.5 m SPICA space mission. We briefly discuss the scientific prospects for each of these facilities



Fig. 13. SOFIA is a Boeing 747 SP modified to carry an open port 2.7 m telescope (chopped aperture 2.5 m), that enables routine access to the highest THz frequencies [84]

A. SOFIA

The Stratospheric Observatory for Infrared Astronomy (SOFIA) contains a 2.5 m telescope in a modified Boeing 747 SP [84] (Fig. 13). Like CCAT, SOFIA is a readily accessible evolving observatory under which we may develop the next generation of instrumentation, taking advantage of the latest technologies. A THz image slicing spectrometer, FIFI-LS is developed for SOFIA, and will be deployed in 2012 [85]. FIFI-LS is similar in many respects to PACS, but the SOFIA facility is better optimized for mapping experiments, so that for FIFI-LS/SOFIA we may expect, for example, large format mapping programs of nearby resolved galaxies revealing the roles of spiral arms and bars in compression of the ISM and ignition of the next generation of star formation in spiral galaxies. New THz spectrometers will be deployed in future years on SOFIA including heterodyne arrays, and bolometer based direct detection systems enabling new science. After Herschel cryogenics expire, and before SPICA is launched, SOFIA will be the only facility from which high frequency THz observations can be made.

B. CCAT

CCAT is a 25 m submm telescope under design by a consortium of universities led by Cornell University that includes Cornell, Caltech, the Universities of Colorado, Bonn, and Cologne, and a consortium of Canadian Universities [86]. CCAT is to have an exceptionally good surface ($10 \mu\text{m}$ RMS), and to be sited near the peak of Cerro Chajnantor in the northern Atacama desert, at an elevation of 5600 m so that CCAT will deliver exceptional sensitivity in the submm bands. Wide-field surveys in the THz continuum with CCAT promise to nearly fully resolve the THz background radiation into its constituent sources. In a 2 year survey, CCAT will detect hundreds of thousands of galaxies and thereby enabling statistically significant studies of star formation to redshifts approaching 10, thereby looking back into time to within 500 million years of the Big Bang. These continuum surveys will discover the sources, but to fully understand the star – *and galaxy* – formation process in the early Universe will require direct detection spectroscopy in the various lines as outlined above. This is surprisingly straight-forward. The observed brightness of the [CII] line in redshift 1-2 star forming galaxies [8] is consistent with a [CII] to underlying THz dust continuum ratio of 10:1. Since continuum sensitive cameras will have bandwidths of 10%, or $\text{RP} \sim 10$, and grating

spectrometers optimized for line detection have $RP \sim 1000$, the

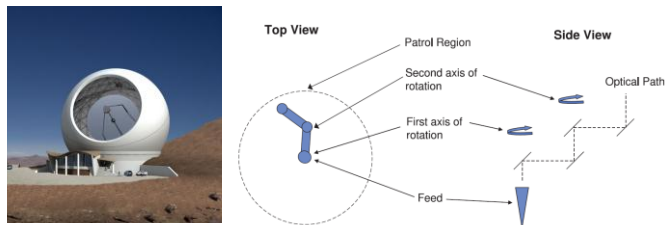


Fig.14. (left) CCAT concept. (right) Simple rotating periscope design for converting a long slit, or stacked Z-Spec-like spectrometer into a multi-object spectrometer. Each beam is coupled into the focal plane by the periscope design, and assigned a “patrol-area” of the focal plane [89].

sensitivity ratio is $(1000/10)^{1/2} = 10$. Therefore, it is as easy to detect the [CII] line as it is the underlying continuum, provided the source redshift falls into the telluric windows. CCAT should detect 1000's of galaxies per square degree in [CII] and other THz fine-structure lines. For detection of sources with unknown redshifts, very large bandwidths (BW) are desired. This can be achieved with free space grating spectrometers in low (1st or 2nd) order, or a THz version of Z-Spec. Z-Spec is a mm wave direct detection spectrometer that achieves very broad detection BW using a curved diffraction grating in a parallel-plate waveguide [87-88]. Either system can deliver detection $BW \sim v/2$ with good optical efficiency. Since sources will be detected at the confusion limit on the sky a multi-object direct detection spectrometer is of importance. Simple concepts for feeding multiple beams into spectroscopes exist. For example, a quasi-optical design involving twin elbowed periscopes [89] (Fig. 14), could feed >10 beams into a long slit spectrometer, or a stack of Z-Spec like spectrometers thereby creating a multi-object system.

Due to its large aperture, exceptional surface, exceptional site, and the use of very broad BW direct detection multi-bam spectrometers, CCAT can detect THz lines from distant galaxies at the rate of tens per hour. Once detected, particularly interesting sources can be delivered to ALMA (see below) for follow-up observations with its exquisite velocity resolved imaging capabilities.

C. SPICA

SPICA is a 3.2 m telescope cooled to below 6 K to be launched by JAXA as early as 2020. With its large, very cold aperture in space, SPICA promises to deliver unrivaled sensitivity in the high frequency THz bands. At present the SAFARI spectrometer to be delivered by ESA is the baseline THz spectrometer [90]. SAFARI covers the 30-210 μm band with tunable $RP \sim 10$ to 10,000 using a Mach-Zehnder imaging FTS, and should deliver sensitivities 20 to 30 times better than PACS/Herschel. There may also be an instrument from NASA on SPICA. A concept based on wave-guide spectrometers together with TES bolometers, called BLISS is under study [91]. BLISS will operate in the 35 to 430 μm regime. The goal is for BLISS to come within a factor of two of the background limit determined by cosmic backgrounds at a $RP \sim 700$. This would yield point source sensitivities 300 times better than Herschel, opening up the most distant galaxies for spectroscopic study in the THz bands. For instance,

BLISS/SPICA should be able to detect the [OI] 63 μm line emission from a ULIRG galaxy at $z = 6$, or to within 1 Gyr of the Big Bang.

D. ALMA

The Atacama Large Millimeter/Submillimeter Array (ALMA) is an international collaboration between Europe, East Asia, and North America in cooperation with the Republic of Chile to build a large interferometer on the Chajnantor plateau in the Atacama Desert in northern Chile. A primary science goal is detection of the [CII] line from a Milky Way-like galaxy at $z \sim 5$ in less than 24 hours observing time. When completed ALMA will consist of 54-12 m and 12-7m high surface accuracy antennas linked for interferometry. Its exceptionally high (5000 m elevation) and dry site enables routine observations in the short submm bands. Ultimately ALMA will have receivers operating from 84 GHz to 920 GHz, divided into 8 bands based on technology and telluric window matches. When complete, each ALMA antenna will be equipped with 8 very low noise receivers (e.g. [60-61]). With the enormous collecting area, low T_{rec} and baselines as long as 16 km, ALMA will achieve unmatched sensitivity in its bands, for line detection at spatial resolutions as small as 6 milli-arcsec at 675 GHz. Early science programs involving 16 antennas operating in bands 3, 6, 7 and 9 are to begin in the fall of 2011.

REFERENCES

- [1] Oberst, T.E., et al. 2006 ApL, 652, L125
- [2] Rubin, R. Rubin, R. H. 1985, ApJSS, 57, 349
- [3] Ferkinhoff, C. et al. 2011, in prep.
- [4] Hollenbach, D.J., & Tielens, A.G.G.M. 1999, Rev. Mod. Phys., 71, 173
- [5] Wolfire M.G., Tielens, A.G.G.M., & Hollenbach, D. 1990, ApJ, 358, 116
- [6] Stacey, G.J., Geis, N., Genzel, R., Lugten, J.B., Poglitsch, A., Sternberg, A. & Townes, C.H. 1991, ApJ, 373, 423
- [7] Hailey-Dunsheath, S.D., Nikola, T., Stacey, G.J., Oberst, T.E., Parshley, S.C., Benford, D.J., Staguhn, J.G., & Tucker, C.E. 2010, ApJL, 714, L162
- [8] Stacey, G.J., Hailey-Dunsheath, S., Ferkinhoff, C., Nikola, T., Parshley, S.C., Benford, D.J., Staguhn, J.G., & Fiolet, N. 2010, ApJ, 724, 957
- [9] Stacey, G.J., Viscuso, P.J., Fuller, C.E., & Kurtz, N.T. 1985, ApJ, 289, 803
- [10] Wright, E.L., et al. 1991, ApJ, 381, 200
- [11] Luhman M.L., Satyapal, S., Fischer, J., Wolfire, M.G., Sturm, E., Dudley, C. Lutz, D. & Genzel, R. 2003, ApJ, 594, 758
- [12] Wagg, J. Carilli, C.L., Wilner, D.J., Cox, P., De Breuck, C., Menten, K., Riechers, D.A., & Walter, F. 2010, A&A, 519, L1
- [13] Brauher, J.R., Dale, D.A., & Helou, G. 2008, ApJSS, 178, 280
- [14] Bradford, C.M., Nikola, T., Stacey, G.J., Bolatto, A.D., Jackson, J.M., Savage, M.L., Davidson, J.A., & Higdon, S.J. 2003, ApJ, 586, 891
- [15] Hailey-Dunsheath, S., Nikola, T., Stacey, G.J., Oberst, T.E., Parshley, S.C., Bradford, C.M., Ade, P.A.R., & Tucker, C.E. 2008, ApJL, 689, L109
- [16] Papadopoulos, P., Isaak, K., & van der Werf, P. 2010, ApJ, 711, 757
- [17] Nikola, T., Hailey-Dunsheath, S., Stacey, G.J., Oberst, T.E., Benford, D. Staguhn, J.G., & Tucker, C.E. 2011, in prep.
- [18] Harris, A.I., Stutzki, J., Graf, U.U., Russell, A.P.G., Genzel, R., & Hills, R.E. 1992, ApJ, 382, L75
- [19] Ward, J.S., Zmuidzinas, J., Harris, A.I., & Isaak, K.G. 2003, ApJ, 587, 171
- [20] Petrosian, V. 1970, ApJ, 159, 833
- [21] Dalgarno, A. and McCray, R. 1972, ARAA, 10, 375.
- [22] Simpson, J.P. 1973, PASP, 85, 470

- [23] Ward, D.B., Dennison, B., Gull, G., and Harwit, M., 1975, *ApJ*, 202, L31.
- [24] Melnick, G., Gull, G.E., & Harwit, M. 1978, *ApJ*, 222, L137
- [25] Melnick, G., Gull, G.E., & Harwit, M. 1979, *ApJ*, 227, L29
- [26] Stacey, G.J., Smyers, S.D., Kurtz, N.T., & Harwit, M. 1983, *ApJ* 265, L7
- [27] Russell, R.W., Melnick, G., Gull, G.E., & Harwit, M. 1980, *ApJ*, 240, L99
- [28] Moorwood, A.F.M., Baluteau, J.-P., Anderegg, M., Coron, N., Biraud, Y., & Fitton, B. 1980, *ApJ* 238, 565
- [29] Colgan, S.W.J., Haas, M.R., Erickson, E.F., Rubin, R.H., Simpson, J.P., & Russell, R.W. 1993, *ApJ*, 413, 237
- [30] Phillips, T.G., Huggins, P.J., Kuiper, T.B.H., & Miller, R.E. 1980, *ApJ*, 238, L103
- [31] Jaffe, D.T., Harris, A.I., Silber, M., Genzel, R., & Betz, A.L. 1985, *ApJ*, 209, L59
- [32] Shibai, H., et al. 1991, *ApJ*, 374, 522
- [33] Furniss, I., Jennings, R.E., King, K.J., Lightfoot, J.F., Emery, R.J., Naylor, D.A., & Fitton, B. 1983, *MNRAS*, 202, 859
- [34] Watson, D.M., Genzel, R., Townes, C.H., Werner, M.W., & Storey, J.W.V. 1984, *ApJ*, 279, L1
- [35] Crawford, M.K., Genzel, R., Townes, C.H., & Watson, D.M. 1985, *ApJ*, 291, 755
- [36] Madden, S.C., Geis, N., Genzel, R., Herrmann, F., Jackson, J., Poglitsch, A., Stacey, G.J., & Townes, C.H. 1993, *ApJ*, 407, 579
- [37] Duffy, P.B., Erickson, E.F., Haas, M.R., & Houck, R.J. 1987, *ApJ*, 315, 68
- [38] Carral, P., Hollenbach, D., Lord, S.D., Colgan, S.W.J., Haas, M.R., Rubin, R.H., & Erickson, E. 1994, *ApJ*, 423, 223
- [39] Lord, S.D., Hollenbach, D.J., Haas, M.R., Rubin, R.H., Colgan, S.W.J., & Erickson, E.F. 1996, *ApJ*, 465, 703
- [40] Barvainis, R., Maloney, P., Antonucci, R., & Alloin, D., 1997, *ApJ*, 484, 695
- [41] Gonzalez-Alfonso, E., Smith, H.A., Fischer, J. & Chernicharo, J. 2004, *ApJ*, 613, 247
- [42] Skinner, C.J., Smith, H.A., Sturm, E., Barlow, M.J., Cohen, R.J., & Stacey, G.J. 1997, *Nature*, 386, 472
- [43] Storey, J.W.V., Watson, D.M., & Townes, C.H. 1981, *ApJL*, 244, L27
- [44] Stacey, G.J. Lugten, J.B., & Genzel, R. 1987, *ApJ*, 313, 859
- [45] Lugten, J.B. 1987, PhD Thesis, University of California, Berkeley
- [46] Colbert, J.W., et al. 1999, *ApJ*, 511, 721
- [47] Genzel, R., et al. 1998, *ApJ* 498, 579
- [48] Van der Werf, P. et al. 2010, *A&A*, 518, L42
- [49] Meijerink, R., Spaans, M., & Israel, F.P. 2007, *ApJ*, 668, 815
- [50] Puget, J.-L., Abergel, A., Bernard, J.-P., Boulanger, F., Burton, W.B., Desert, F.-X., Hartmann, D., 1996, *A&A*, 308, L5
- [51] Fixsen, D. J, Dwek, E., Mather, J. C., Bennett, C. L. & Shafer, R. A., 1998, *ApJ*, 508, 123
- [52] Devlin, M.J., et al. 2009, *Nature*, 458, 737
- [53] Smail, I., Chapman, S.C., Blain, A.W., & Ivison, R.J., 2004, *ApJ*, 616, 71
- [54] Weiß, A., Henkel, C., Downes, D., & Walter, F. 2003, *A&A*, 409, L41
- [55] Maiolino, R., et al. 2005, *A&A* 440, L51.
- [56] Iono, D., et al. 2006, *ApJ*, 645, L97
- [57] Maiolino, R., Caselli, P., Nagao, T. Walmsley, M., De Breuck, C., & Meneghetti, M. 2009, *A&A*, 500, L1
- [58] Ferkinhoff, C., Hailey-Dunsheath, S.D., Nikola, T., Parshley, S.C., Stacey, G.J., Benford, D.J., & Staguhn, J.G. 2010, *ApJ*, 714, L147
- [59] Sturm, E. et al. 2010, *A&A*, 518, L36
- [60] Risacher, C. et al., 2006, *A&A*, 454, L17
- [61] Baryshev, A.M., et al. 2008, in Proceedings of the Nineteenth International Symposium on Space Terahertz Technology, Wolfgang Wild Ed., 258 (2008)
- [62] Weidner, M.C. et al. 2007, IAU Symposium #237, Cambridge University Press, 495
- [63] GREAT instrument sensitivity found at:
http://www.sofia.usra.edu/Science/instruments/instruments_great.html
- [64] Bradford, C.M. 2001 PhD Thesis, Cornell University
- [65] Hailey-Dunsheath, S. 2009, PhD Thesis, Cornell University
- [66] Jacquinet, P. 1954, *Journal of the Optical Society of America*, 44, 761
- [67] Watson, D.M. 1982, PhD thesis, University of California, Berkeley
- [68] Bradford, C.M., Stacey, G.J., Swain, M.R., Nikola, T., Bolatto, A.D., Jackson, J.M., Savage, M.L., Davidson, J.A., & Ade, P.A.R. 2002, *Appl. Opt.* 41, 2561
- [69] Oberst, T.E. 2009, PhD Thesis, Cornell University
- [70] Stacey, G.J., Beeman, J.W., Haller, E.E., Geis, N., Pogitsch, A. & Rumitz, M. 1992, *IJIMW*, 13, 1689
- [71] PACS online observing manual
http://www.iac.es/proyecto/herschel/pacs/pacs_om.pdf
- [72] Reike, G. H. 1994, "Detection of Light from the Ultraviolet to the Submillimeter", Cambridge University Press, ISBN 0521410282
- [73] Bradford, C.M., Stacey, G.J., Nikola, T., Bolatto, A.D. Jackson, J.M., Savage, M.L., & Davidson, J.A. 2005, *ApJ.*, 623, 866
- [74] Brisbin, D. et al. 2011, in prep.
- [75] Yngvesson, S., et al. 2004, in 15th Int. Symp. Space THz Technology, ed. G. Narayanan, 365
- [76] Ferkinhoff, C. Nikola, T., Parshley, S.C., Stacey, G.J., Irwin, K.D., Cho, H-M., & Halpern, M. 2010, *SPIE*, 7741, E.26F
- [77] Poglitsch, A., et al. 2010, *A&A* 518, L2
- [78] Gracia-Carpio, J., et al. 2011 *ApJ*, 728, L7
- [79] Sturm, E., et al. 2011, accepted for publication in *A&A*
- [80] Griffin, M., et al. 2010, *A&A*, 518, L3
- [81] Turner, A.D., et al. 2001, *Appl. Opt.* 40, 4921
- [82] Gonzalez-Alfonso, E. et al. 2010, *A&A*, 518, L43
- [83] Ivison, R. J., Papououlos, P.P., Smail, I., Greve, T.R., Thomson, A.P., Xilouris, E.M., & Chapman, S.C., 2010, *A&A*, 518, L31
- [84] Becklin, E. E., & Gehr, R.D. 2009, *SPIE*, 7453, 745302
- [85] Klein, R., et al. 2010, *SPIE* 7735, 77351T
- [86] Giovanelli, R., Carpenter, J., Radford, S. Sebring, T., Soifer, T., Stacey, G., Zmuidzinas, R., et al. Astro2010 White Paper
<http://www.submm.org/sci/astro2010/Giovanelli-CCAT.pdf>
- [87] Bradford, C.M., et al. 2004, *SPIE*, 5498, 257
- [88] Bradford, C.M., et al. 2009, *ApJ*, 705, 112
- [89] Goldsmith, P.F., & Seiffert, M. 2009, *PASP*, 121, 735
- [90] Swinyard, B. et al. 2008, *SPIE*, 7010, 70100I
- [91] Bradford, C.M. et al. 2010, *SPIE*, 7731, 77310S